

Spectrum from Defocus: Fast Spectral Imaging with Chromatic Focal Stack

M. Kerem Aydin^{1,*} Yi-Chun Hung^{1,*} Jaclyn Pytlarz² Qi Guo³ Emma Alexander^{1,4,†}

¹Department of Computer Science, McCormick School of Engineering, Northwestern University

²Dolby Laboratories, Inc.

³Elmore Family School of Electrical and Computer Engineering, Purdue University

⁴Center for Robotics and Biosystems, McCormick School of Engineering, Northwestern University

* Equal contribution

ealexander@northwestern.edu

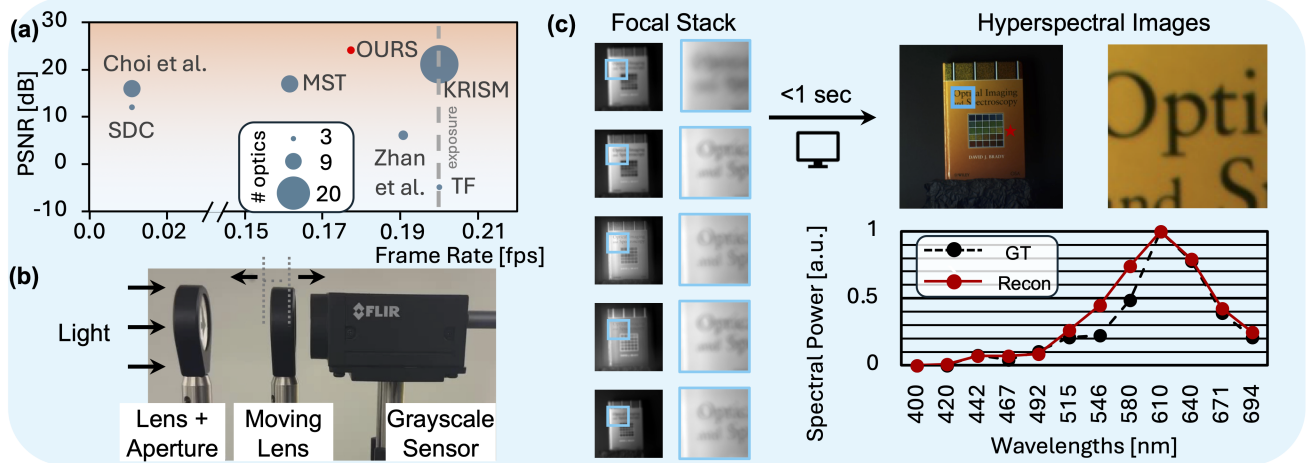


Figure 1. **Comparison and overview of our Spectrum from Defocus (SfD) camera.** (a) Our camera provides state-of-the-art PSNR with simple optics and a high frame rate, which we compute as $1/(t_{\text{exposure}} + t_{\text{compute}})$ with a simulated 5 sec total exposure for each method. Bubble diameters correspond to the number of optical components in each method. See Table 1 for details. (b) Our hardware prototype uses a moving lens to change the focus of chromatically aberrated light on its way to a grayscale sensor. (c) Our imaging system captures a grayscale focal stack and reconstructs images in under a second. We show an RGB projection of a 12-channel recovered image, with a high-resolution inset (blue square) and reconstructed spectrum (red star).

Abstract

Hyperspectral cameras face harsh trade-offs between spatial, spectral, and temporal resolution in an inherently low-photon regime. Computational imaging systems break through these trade-offs with compressive sensing, but require complex optics and/or extensive compute. We present *Spectrum from Defocus (SfD)*, a chromatic focal sweep method that recovers state-of-the-art hyperspectral images with a small system of off-the-shelf optics and < 1 second of compute. Our camera uses two lenses and a grayscale sensor to preserve nearly all incident light in a chromatically-aberrated focal stack. Our physics-based iterative algorithm efficiently demixes, deconvolves, and denoises the blurry grayscale focal stack into a sharp spectral image.

The combination of photon efficiency, optical simplicity, and physical modeling makes SfD a promising solution for fast, compact, interpretable hyperspectral imaging.

1. Introduction

Hyperspectral imaging (HSI) extends traditional color imaging by capturing detailed spectral signatures across numerous spectral bands, rather than just the three broad RGB bands. This richer spectral information is essential for applications that rely on subtle material differences, such as remote sensing for environmental monitoring [3], medical diagnostics [20], food quality control [11], and material identification in industrial inspection [24]. Despite its im-

portance, capturing high-quality spectral images with compact, affordable cameras remains challenging. Hyperspectral sensors suffer from inherently lower signal-to-noise ratios because incoming light is divided across many spectral channels, leaving each channel with reduced photon counts. This challenge is reflected in systems that rely on dispersive elements [32], which spread spectral information to the corresponding sensor pixels. This limitation makes traditional hyperspectral cameras particularly fragile in low-light conditions or dynamic scenes that require short exposure times, limiting their practicality.

To mitigate this fragility, CASSI-like computational imaging systems have been introduced [13, 19, 28]. These systems encode spectral information into the spatial dimension using a coded aperture [28] and employ an optimization framework in the reconstruction phase. However, solving optimization problems in hyperspectral imaging entails high computational demands due to extensive matrix multiplications in iterative processes and may require large-scale matrix inversion. Although adopting a naive optimization algorithm (e.g., inverse filtering as used by Zhan et al.) can reduce computational complexity, it often degrades the quality of reconstructed images, limiting applicability to real-world data.

Data-driven methods [5, 21] have been proposed in conjunction with CASSI-like imaging systems for addressing the computational issues. These methods typically design parameterized modules to capture the intrinsic low-rank properties in both spatial and spectral dimensions. For instance, MST [5] introduces Spectral-wise Multi-head Self-Attention (S-MSA) to exploit spectral-wise similarity in hyperspectral image reconstruction. However, the hallucination [12] issue in data-driven models can restrict their applicability in tasks requiring precise spectral accuracy, such as material analysis and food quality control.

Considering these limitations—light inefficiency, high computational complexity, and hallucination—we propose a chromatic focal sweep camera consisting of two lenses and a grayscale sensor. The special sensing matrix structure in our physics-based iterative algorithm enables the reconstruction of high-quality and robust hyperspectral images. Furthermore, the physics-based approach mitigates the hallucination issue commonly observed in data-driven methods.

The main contributions of this paper are as follows:

- State-of-the-art spectral image quality through a combination of light-efficient optics and a robust algorithm.
- Fast computation with a physics-based, interpretable model.
- A simple optical design consisting of few, off-the-shelf (OTS) components, which outperforms systems with up to 20 optical elements.

2. Related Works

Scanning Methods acquire hyperspectral data cubes by sequentially capturing individual 2D slices of the scene. The most straightforward implementation uses band-pass filters or liquid crystal tunable filters to capture one narrow spectral band per frame, gradually scanning across the spectrum [27]. Pushbroom systems take a slightly different approach, capturing a single spatial row at a time through a narrow slit, while dispersive optics spread each row into a full spectrum across the sensor [25]. While these techniques can deliver high spatial and spectral resolution, they suffer from low photon efficiency—since only a fraction of the incoming light is used for each measurement—and long acquisition times, which restricts them to static, well-lit scenes. In contrast, our method passively encodes spectral information into each frame and avoids light-blocking (low light transmission) elements entirely, enabling faster capture with higher photon efficiency.

Compressive hyperspectral imaging systems capture optically coded measurements that must be computationally reconstructed to recover the final hyperspectral data cube. Among these, Coded Aperture Snapshot Spectral Imaging (CASSI) [28] was developed to overcome the limitations of sequential spectral scanning systems. A coded aperture is placed either before or after a dispersive prism in the optical path, encoding spectral signatures into the spatial domain. CASSI systems are typically divided into two categories based on their encoding strategy: spatially-encoded CASSI, which employs a single disperser (SD-CASSI) [28], and spatial-spectral CASSI, which codes information in both spatial and spectral domains (DD-CASSI [13], SS-CASSI [19]). Regardless of the encoding scheme, in all CASSI systems reconstruction algorithms play a critical role in determining final image quality. Early reconstruction methods relied on optimization-based solvers with hand-crafted priors [28], while more recent approaches introduced learning-based reconstructions [5, 22]. Hybrid methods further combined the system’s sensing matrix with deep learning, either to directly parameterize the solution space [9] or to learn data-driven priors for regularization [29]. Despite their success, traditional CASSI systems are often relatively large, and mechanically sensitive, making them impractical for compact imaging platforms. In contrast, our system requires only two off-the-shelf lenses and achieves spectral imaging through a focal sweep, significantly reducing hardware complexity.

Another class of compressive spectral imagers relevant to this work are spectral-diffractive imagers, which encode spectral information using diffractive optical elements (DOEs) with optimized phase masks, followed by computational reconstruction to recover the hyperspectral data cube. Early work, such as [14], used simple diffraction gratings to simultaneously resolve spatial and spectral in-

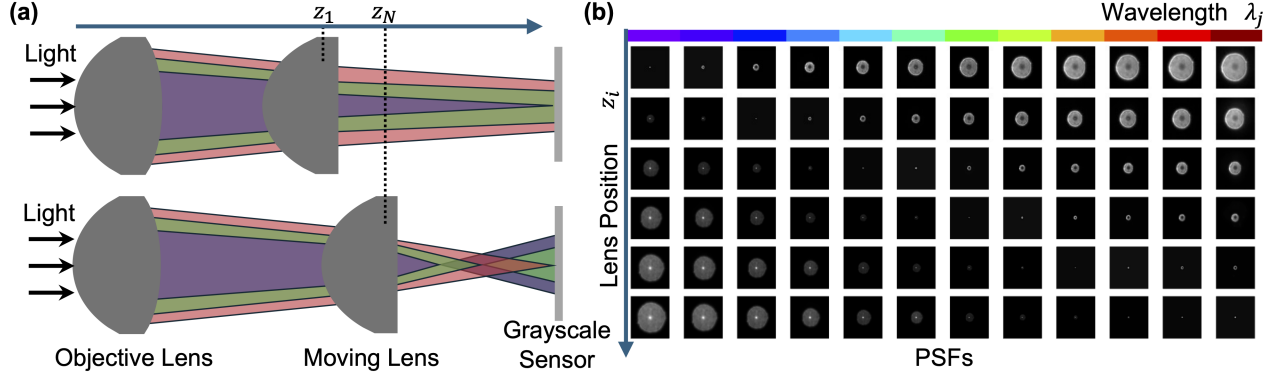


Figure 2. **Optical design.** (a) The system consists of a lens pair in which the second lens is moved to N positions, z_1, z_2, \dots, z_N , respectively when capturing N images of a scene. We assume the imaging target is within the depth of field throughout this paper. The N captured images, I_1, \dots, I_N , individually focus N discrete, predetermined wavelengths, $\lambda_1, \dots, \lambda_N$, while blurring others, forming a chromatic focal stack. (b) Measured point spread functions (PSFs) of the real-world prototype at different wavelengths λ_i and lens position z_i . The PSFs clearly show the chromatic focal shift, as the focus shifts to different wavelengths at different lens positions z_i . Although six different lens positions are shown, only a subset of lens positions is used during reconstruction, corresponding to the number and location of captured measurements.

formation, but these systems suffered from low resolution and bulky optical assemblies. Later, Heide et al. [16] introduced a co-designed pair of DOEs with optimized phase profiles, enabling tunable control over both focus and chromatic aberration without the need for large, conventional optics. They further proposed a blind deconvolution algorithm to jointly recover the scene and correct for encoding imperfections, improving robustness. More recently, efforts have focused on using a single DOE, reducing hardware complexity but introducing stronger optical artifacts which are typically handled through end-to-end deep learning reconstructions trained on large spectral datasets. Similar to these approaches, our system also relies on spectrally encoded PSFs; however, in contrast, we achieve this encoding using the naturally occurring chromatic aberration of standard refractive lenses, alleviating the need for custom-fabricated optics.

Recent Spectral Computational Imagers highlight a trade-off between optical simplicity and computational cost in spectral imaging. Spectral DiffuserCam (SDC) [23] uses a lensless design with a spectral filter array, but requires solving a computationally expensive inverse problem via FISTA. In contrast, KRISM [26] employs a complex optical system to directly measure the spectral singular values, offloading most of the computation to the hardware itself. Our work balances both approaches, combining a simple optical setup using off-the-shelf lenses with a lightweight, physics-based reconstruction.

Spectral Focal Sweeping and Stacking refers to techniques that capture images at multiple focus distances to jointly recover spectral, spatial, or depth information. [10] used uncorrected chromatic aberration to passively extend

depth of field across wavelengths, allowing different colors to focus at different depths. [7] introduced a color-coded aperture, creating different depths of field for each RGB channel and using this as a cue for joint depth estimation and all-in-focus imaging. Both methods leverage chromatic defocus, but only for depth and RGB recovery. [15] modeled spatially-varying chromatic PSFs to correct color fringing in simple lenses, enhancing RGB image quality. In contrast, we preserve and directly exploit chromatic defocus to encode a full spectral cube across the visible range. Finally, [17] proposes a novel multispectral focal stack acquisition method. The system intentionally enhances chromatic aberration while suppressing other optical aberrations, allowing different spectral channels to focus on distinct scene depths enabling recovery of the full light field using an algorithm that fills in the missing details.

3. Method

We aim to reconstruct a hyperspectral image $\mathbf{X} \in \mathbb{R}^{H \cdot W \times C}$ of the target scene using a focal stack $\mathbf{Y} \in \mathbb{R}^{H \cdot W \times N}$, where H , W , and C represent the height, width and channel of the image, respectively. Since N grayscale images in the focal stack are captured by translating the moving lens to different positions z_i (more details in Sec. 3.1), we can express the forward model between \mathbf{X} and \mathbf{Y} as follows:

$$\mathbf{y} = \mathbf{C}\mathbf{H}\mathbf{x} = \mathbf{C} \begin{bmatrix} \mathbf{H}_{1,1} & \dots & \mathbf{H}_{1,C} \\ \vdots & \ddots & \vdots \\ \mathbf{H}_{N,1} & \dots & \mathbf{H}_{N,C} \end{bmatrix} \mathbf{x}. \quad (1)$$

Each block $\mathbf{H}_{i,j} \in \mathbb{R}^{(H+K-1) \cdot (W+K-1) \times H \cdot W}$ is a linear 2D convolutional matrix generated by a PSF

Table 1. **Comparison of SOTA hyperspectral imaging systems** in terms of reconstruction performance, and computational and optical requirements. Reconstruction quality is benchmarked on 30 images from the Harvard dataset [6] and adopt a brightly lit condition with 5-second total exposure time and optical component effects (see supplement). Timings are reported for an NVIDIA RTX A6000. The count of optical components includes: lenses, apertures, prisms, actuators, SLMs, and sensors, but not control electronics.

Modality	Reconstruction Performance			Computation and Optics			Category
	PSNR (dB) \uparrow	SSIM \uparrow	SAM ($^\circ$) \downarrow	Compute Time	FoV ($^\circ$)	Opt. Components	
TF	-4.88	0.03	88.71	0	N.A.	3	Spectral Filter
SDC [23]	12.03	0.37	40.88	> 15 mins	14	3	
MST [5]	<u>21.18</u>	0.53	38.87	1.19 s	10	9	
Choi et al. [9]	15.97	0.41	41.84	> 15 mins	10	9	Dispersive Element
KRISM [26]	21.12	<u>0.58</u>	34.38	0	32	20	
Zhan et al. [31]	6.11	0.04	71.45	0.24 s	10	5	Chromatic Aberration
Ours	24.10	0.61	<u>36.51</u>	0.64 s	10	4	

$\mathbf{K}(z_i, \lambda_j) \in \mathbb{R}^{K \times K}$, associated with the j th channel of \mathbf{X} and wavelength λ_j . The binary matrix $\mathbf{C} \in \mathbb{R}^{N \cdot H \cdot W \times N \cdot (H+K-1) \cdot (W+K-1)}$ is used to crop the targeted region of the convolved result (i.e., $\mathbf{H}\mathbf{x}$), ensuring the same pixel count between \mathbf{x} and \mathbf{y} . Here, we vectorize the images \mathbf{X} and \mathbf{Y} using column-stacking, defining $\mathbf{x} = \text{vec}(\mathbf{X}) := [\mathbf{X}_1^T, \dots, \mathbf{X}_C^T]^T$ and $\mathbf{y} = \text{vec}(\mathbf{Y})$, where \mathbf{X}_j denotes the j th column of the matrix \mathbf{X} . Here, \mathbf{X}_j can also be interpreted as the j th channel of the hyperspectral image.

3.1. System Design

As shown in Fig. 2a, the imaging system comprises an objective lens, a moving lens, and a grayscale sensor. The objective lens and the camera remain fixed while the moving lens is translated to N positions along the optical axis, z_1, \dots, z_N , when capturing the N images in a chromatic focal stack. Given a pre-determined depth of field for the optical system and a set of discrete wavelengths $\lambda_1, \dots, \lambda_N$, we calibrate the i th position of the moving lens z_i so that the i th wavelength λ_i is in focus, as shown by the point spread functions in Fig. 2b. Assuming the system measures a target in the depth of field, the captured image I_i contains sharp textures corresponding to wavelength λ_i . In contrast, textures of other wavelengths gradually blur out as the wavelengths deviate from λ_i . The total travel distance of the moving lens, $z_N - z_1$, is very small compared to the effective focal length of the system. Thus, we assume the magnification of the captured images I_1, \dots, I_N remains constant when capturing the chromatic focal stack.

3.2. Inverse Algorithm

We solve the spectral image recovery problem with an iterative optimization that alternates between inverting the physical forward model in Eq. (1) and applying a data-driven regularizer. Specifically, we modify plug-and-play ADMM [8] with two task-specific augmentations to improve robustness and computational speed. First, we project spectra onto a limited number of principal components, taking advantage

of the low-rank statistics of natural visible spectra. Second, we separate the spatial and frequency domain computations for fast matrix inversion.

We formulate a minimization problem in an eigenspace as follows:

$$\min_{\mathbf{z}} \frac{1}{2} \|\mathbf{y} - \mathbf{CHP}\mathbf{z}\|_2^2 + \Phi_{\theta}(\mathbf{P}\mathbf{z}), \quad (2)$$

where $\Phi_{\theta}(\cdot)$ is an off-the-shelf deep-learning-based regularizer with parameters θ . The vector $\mathbf{z} \in \mathbb{R}^{H \cdot W \cdot v}$, where v represents the dimensionality of the selected eigenspace, is utilized to exploit the property that natural visible-range spectra primarily reside in a lower-dimensional space (i.e., $\mathbf{x} \approx \mathbf{P}\mathbf{z}$). We define $\mathbf{P} = \mathbf{B}^T \otimes \mathbf{I}_{HW}$, where the rows of \mathbf{B} , shaped as $\mathbb{R}^{v \times C}$, are eigenvectors obtained from the Harvard dataset [6], as reported in [2]. The matrix \mathbf{I}_{HW} and the operator \otimes denote an identity matrix shaped as $HW \times HW$ and the Kronecker product, respectively.

To adopt a plug-and-play ADMM [8], we transformed Eq. (2) by introducing slack variables \mathbf{v} and \mathbf{u} , and by using the change of variables $\hat{\mathbf{H}} := \mathbf{HP}$:

$$\begin{aligned} \min_{\mathbf{z}, \mathbf{u}, \mathbf{v}} \quad & \frac{1}{2} \|\mathbf{y} - \mathbf{C}\mathbf{v}\|_2^2 + \Phi_{\theta}(\mathbf{u}) \\ \text{s.t.} \quad & \mathbf{v} = \hat{\mathbf{H}}\mathbf{z}, \mathbf{u} = \mathbf{z}. \end{aligned} \quad (3)$$

Followed by the derivation of ADMM (see supplement), we have Algorithm 1 for solving Eq. (3). Here, ξ and η denote dual variables.

Plug-and-play ADMM primarily consists of two main update steps: a **primal variable update** (\mathbf{v} , \mathbf{z} , \mathbf{u}) and a **dual variable update** (ξ and η). In the primal update, \mathbf{v} can be interpreted as a pseudo-measurement estimated from the true measurement \mathbf{y} and the current update \mathbf{z}_i . An estimate of a projected image z_{i+1} is then generated using a Wiener-like filter, $(\mu_1 \hat{\mathbf{H}}^T \hat{\mathbf{H}} + \mu_2 \mathbf{I})^{-1}$. Since this estimate may contain noise, the proposed algorithm further applies an off-the-shelf deep learning denoiser $\phi_{\theta}(\cdot)$ to suppress

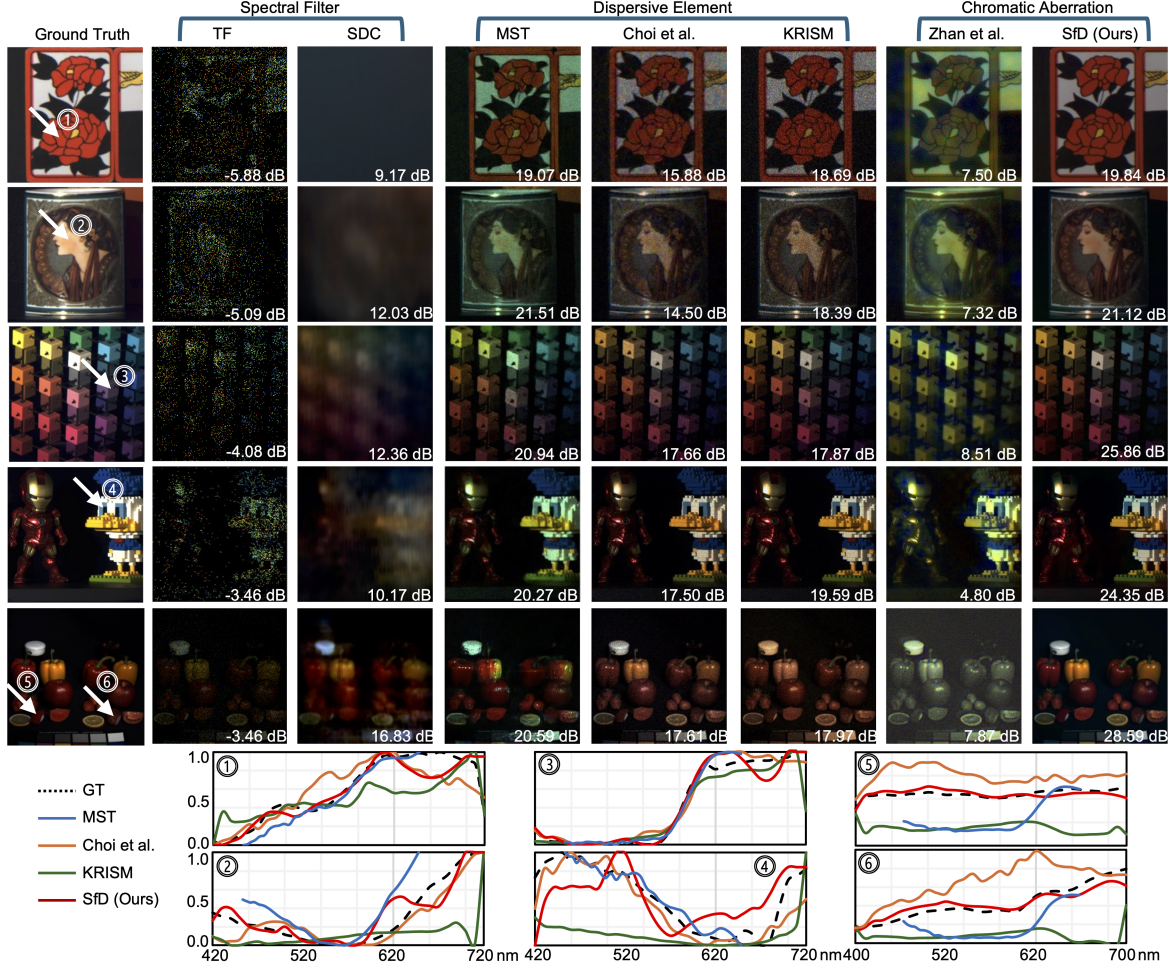


Figure 3. **Comparison of simulated SOTA methods.** We illustrate the performance of several SOTA methods simulated on five hyper-spectral images from the KAIST [9] and CAVE [30] dataset. The PSNR of the reconstructed hyperspectral image is listed for each, below an RGB projection of the data. Our method, using a simulated focal stack of 5 measurements, performs well, with high spatial resolution and no color tinting (compare to MST). Spectra are shown for the numbered points, indicated with white arrows on each image. We reconstruct spectra smoothly and accurately. Note that MST can only reconstruct a limited wavelength range, as its training data spans only 453 – 648 nm.

noise and enhance the result. We applied the denoiser after converting \mathbf{z}_{i+1} back to the image domain, as the off-the-shelf denoiser was trained on data in the hyperspectral image domain [18]. In the dual update, ξ and η are updated by evaluating the residual of the constraints in Eq. (3). By iteratively alternating between primal and dual updates, the algorithm can heuristically converge to produce a projected image, which can then be used to recover a hyperspectral image (i.e., $\mathbf{x} \approx \mathbf{Pz}$). Specifically, we declare convergence when the step size falls below a fixed threshold or exceeds the previous step size scaled by a convergence check parameter. It should be noted that updating \mathbf{z} requires inverting a large, non-diagonal matrix. Given the matrix’s large size, computing its inverse directly is impractical. To overcome this challenge, we derived a fast matrix inversion formula

by leveraging the Block Circulant with Circulant Blocks (BCCB) structure of submatrices in \mathbf{H} (see Supplement). This fast inversion formula enables us to run the Plug-and-play ADMM algorithm, achieving sub-second reconstruction times. As a final step, we correct for the spectral response curve of our grayscale camera and visible light filter.

4. Experimental Results

4.1. System Specifications

We use the Thorlabs LBF254-050-A best-form lens as the objective lens and the Thorlabs AL2550M-A aspherical lens as the focusing lens, both with 50 mm focal lengths. These lenses were chosen based on their measured performance in optical simulations, with particular emphasis on

Algorithm 1 Plug-and-play ADMM Iterative Procedure

```
1: Given:  $\mu_1, \mu_2 > 0$ , and  $\phi_\theta(\cdot)$  as an off-the-shelf deep learning denoiser.  
2: Initialize:  $\mathbf{z}_0 \leftarrow 0.5 \cdot \mathbf{1}$ ,  $\mathbf{u}_0 \leftarrow 0.5 \cdot \mathbf{1}$ ,  $\boldsymbol{\xi}_0 \leftarrow \mathbf{0}$ ,  $\boldsymbol{\eta}_0 \leftarrow \mathbf{0}$   
3: while not converged do  
4:    $\mathbf{v}_{i+1} \leftarrow (\mathbf{C}^T \mathbf{C} + \mu_1 \mathbf{I})^{-1} (\mathbf{C}^T \mathbf{y} + \mu_1 \hat{\mathbf{H}} \mathbf{z}_i - \boldsymbol{\xi}_i)$   
5:    $\mathbf{z}_{i+1} \leftarrow (\mu_1 \hat{\mathbf{H}}^T \hat{\mathbf{H}} + \mu_2 \mathbf{I})^{-1} \left( \hat{\mathbf{H}}^T (\mu_1 \mathbf{v}_{i+1} + \boldsymbol{\xi}_i) \right.$   
      $\left. + (\boldsymbol{\eta}_i + \mu_2 \mathbf{u}_i) \right)$   
6:    $\mathbf{u}_{i+1} \leftarrow \mathbf{P}^T \phi_\theta (\mathbf{P} (\mathbf{z}_{i+1} + \boldsymbol{\eta}_i))$   
7:    $\boldsymbol{\xi}_{i+1} \leftarrow \boldsymbol{\xi}_i + \mu_1 (\mathbf{v}_{i+1} - \hat{\mathbf{H}} \mathbf{z}_{i+1})$   
8:    $\boldsymbol{\eta}_{i+1} \leftarrow \boldsymbol{\eta}_i + \mu_2 (\mathbf{u}_{i+1} - \mathbf{z}_{i+1})$   
9: end while
```

their longitudinal chromatic aberration, which serves as the primary spectral encoding mechanism in our system. The system produces about 1 mm of axial chromatic focal shift across the visible spectrum, with a 34 cm depth of field (2.64 – 2.98 m). Longitudinal chromatic aberration dominates spherical by a factor of 6, and other aberrations are small. See supplement for a detailed description of the optics.

To calibrate the PSFs at different lens position and target wavelengths, we imaged a point source at 2.8 m through a set of 12 visible bandpass filters with central wavelengths spanning 400 to 694 nm. Fig. 2b shows the PSF, $\mathbf{K}(z_i, \lambda_j)$, at several lens positions z_i for each wavelength λ_j . We collect PSFs at 12 lens positions, corresponding to an in-focus image for each waveband. For each reconstruction, we use the PSFs for all 12 wavebands and only the subset of lens positions used in the measurements. We assume the target to be within the depth of field and ignore defocus in the image formation, see Fig. 5a and supplement for defocus effects.

4.2. Synthetic Experiments

We evaluated the performance of our SfD camera on there publicly available hyperspectral image datasets [4, 9, 30] and compare to several state-of-the-art methods. Photon noise was simulated for all methods using a Poisson process. Specifically, we assume a brightly lit scene with a photon flux of $4.6 \cdot 10^{17} \text{m}^{-2} \text{s}^{-1}$ in the visible range.

To ensure a fair comparison across different modalities, we configured a total exposure time of 5 seconds (i.e., number of exposures \times duration per exposure) for all modalities and maintained the same brightness conditions as described above. Notably, under this configuration, increasing the number of exposures does not result in a longer total exposure time. We also accounted for the blocking and absorption effects of optical components in each modality (see supplement). Additionally, we assumed an ideal camera with negligible transition time between exposures, infi-

nite dynamic range, no quantization error, and zero readout noise.

As shown in Tab. 1, our method outperforms others in PSNR and SSIM while achieving second place in SAM. Compared to our SfD camera, tunable-filter (TF) methods and SDC exhibit lower light efficiency due to spectral filters blocking a significant portion of incoming photons. The performance of data-driven methods, such as MST and Choi et al., degrades when the noise in the training data does not align with the noise encountered during evaluation. Conversely, KRISM and Zhan et al.’s work lack spatial denoising modules, leading to inferior performance under photon-limited conditions. Noted that KRISM achieves the highest SAM performance, as it is capable to conduct singular value decomposition in the individual scene. Additionally, the algorithm used in [31] is an naive inverse filtering, which can be extremely unstable in the noisy condition.

In terms of computation and optics, our SfD camera achieves a well-balanced trade-off while delivering SOTA reconstruction performance. Although KRISM offloads computational complexity to optics, its bulky system limits applicability in portable devices. Similarly, while MST ranks second in PSNR performance, it requires approximately twice the computational time and a greater number of optical components.

As shown in Fig. 3, our SfD camera demonstrates superior reconstruction quality in low spatial-frequency regions, such as the white background of the flower and the gray background of the mug. Due to our physics-based iterative algorithm, our SfD camera exhibits minimal hallucination artifacts, as evidenced by a comparison of the yellow pepper patches in MST and our method. Notably, although Zhan et al. employ chromatic aberration in a manner similar to our approach, their inverse-filtering algorithm is highly sensitive to noise, resulting in inferior color reconstruction.

Fig. 3 also shows spectra at 6 indicated pixels, illustrating our successful high dimensional reconstructions across multiple datasets. Notably, points 5 and 6 demonstrate a metamer case between real and fake food items. Unlike the other methods, SfD is able to match both of these spectra well, providing the key material-differentiation advantage of hyperspectral imaging over conventional RGB imaging [11]. Note that the data-driven technique MST fails the most seriously on distinguishing between these spectra, as seen previously in [12].

4.3. Experiments on Real Data

We built a prototype camera according to the description in Sect. 3.1, shown in Fig. 1b. We imaged and reconstructed several real scenes, with data and code publicly available on our GitHub page.

Objects were placed at a distance of 2.8 meters from the camera, at which depth our camera has a theoretical depth

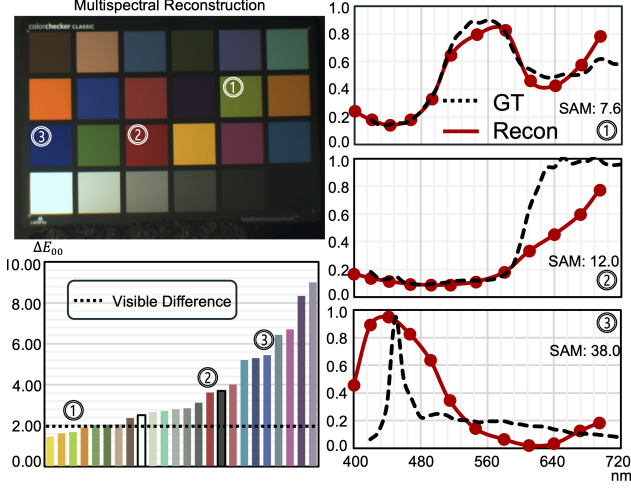


Figure 4. **Quantitative evaluation on real data.** We reconstruct the Macbeth color chart from a 5-measurement focal stack to evaluate hyperspectral and trichromatic reconstruction quality. The spectral reconstruction of the full image with three spectra from RGB patches and the ΔE_{00} perceptual error of each square are presented. The SAM in degree is also reported for the RGB color patches.

of field of 34 cm. Additionally, to evaluate light efficiency of the SfD camera, our illuminating light source delivers approximately 25 lux, which is about 15 times smaller than common indoor brightness condition [1]. We ensured that all test targets remained within the abovementioned depth of field to minimize the optical defocus caused by the depth change.

In addition to keeping the targets within the depth of field, positioning them close to the optical axis helps mitigate focal length variations caused by spherical aberration and minimizes lateral chromatic aberration. These optical effects, which are not modeled in our SfD algorithm, remain a source of model mismatch. To minimize their impact on our reconstruction algorithm, we center-crop the image around the test target, where the optical system performs closest to ideal.

4.3.1. Quantitative Evaluation

To assess the spectral accuracy and trichromatic color quality of our SfD algorithm, we imaged the standard Macbeth color chart, shown in Fig. 4. For spectral accuracy evaluation, we sampled a pixel from each RGB color patch in the reconstruction. We then used the Spectral Angle Mapper (SAM) to compare each sample’s spectral accuracy to the known reflectance of the patch, adjusted by the scene’s illuminance spectrum. The reconstructed image and three example spectral curves are shown in Fig. 4. The SfD camera accurately reconstructs the image and captures the overall spectral trend in the selected samples. However, its perfor-

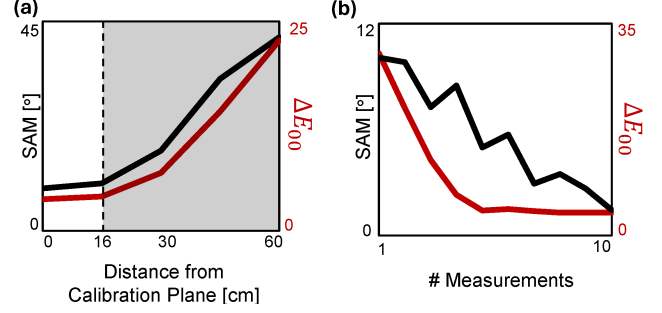


Figure 5. **Robustness of Color Checker Recovery.** (a) We assess the reconstructed spectral accuracy at varying distances from the calibration plane. Compared to the theoretical working distance of 16 cm from the calibration plane, mild deviations from this range do not significantly impact the results. (b) We evaluate spectral accuracy as a function of the number of measurements. Adding measurements (which in the real data setting corresponds to a longer total exposure time), improves reconstruction, with performance saturating more quickly in RGB than in spectrum. See supplement for corresponding images.

mance degrades in the longer wavelength range (> 600 nm) due to the lower scene illuminance in this range, resulting in a reduced signal-to-noise ratio (SNR).

Additionally, we characterize the accuracy of color reproduction with respect to human vision in terms of the perceptual color difference metric, ΔE_{00} [1], as follows. First, we model the known Macbeth chart reflectances $R(\lambda)$ as our ground truth reference spectra $S_{GT}(\lambda) = R(\lambda)$. We then project this ground truth spectra $S_{GT}(\lambda)$ into the CIE XYZ color space by multiplying and integrating over the human color matching functions $\bar{x}, \bar{y}, \bar{z}$:

$$\begin{bmatrix} X \\ Y \\ Z \end{bmatrix} = \begin{bmatrix} \alpha_x \int \bar{x}(\lambda) S(\lambda) d\lambda \\ \alpha_y \int \bar{y}(\lambda) S(\lambda) d\lambda \\ \alpha_z \int \bar{z}(\lambda) S(\lambda) d\lambda \end{bmatrix} \quad (4)$$

where α_i is a normalization factor. We repeat this spectra-to-XYZ process with our reconstructed spectra $S_{CfD}(\lambda)$. For the purposes of this application, where low luminance reflective surfaces are being evaluated, we use the perceptual difference metric ΔE_{00} , which measures differences in the $L^*a^*b^*$ color space. We use the XYZ of the white patch as our adapting white point during conversion to $L^*a^*b^*$. To reduce the effects of non-uniform illumination in our scene and to especially highlight spectral color quality difference, the luminance between the two colors was first normalized before evaluating the color difference:

$$XYZ_{CfD} = XYZ_{CfD} \cdot Y_{GT} / Y_{CfD}, \quad (5)$$

$$\Delta E_{00} = (XYZ_{GT}, XYZ_{CfD}; XYZ_P). \quad (6)$$

The ΔE_{00} values for each of the 24 Macbeth color checker squares are shown in Fig. 4. A ΔE_{00} value at or

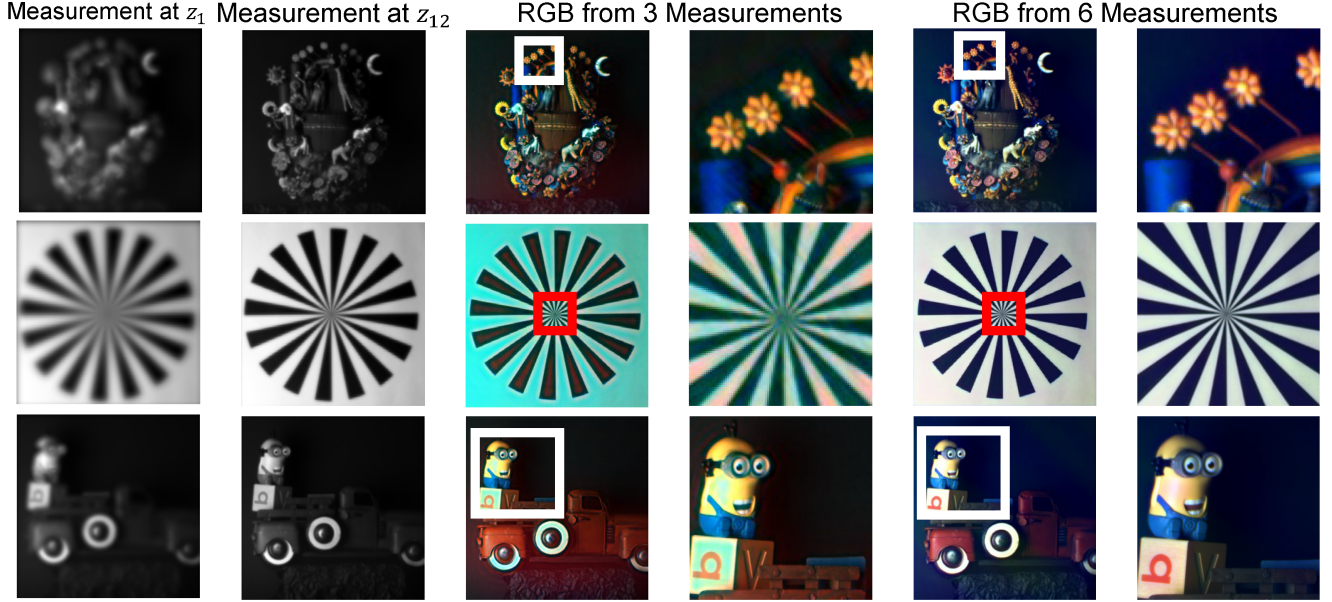


Figure 6. **Qualitative results on real data.** Measurements from our grayscale camera show significant blur (left). Reconstructing color from a three-measurement focal stack (middle) leads to spatial and spectral artifacts that can be resolved by including additional measurements (right).

below 2 is considered perceptually equivalent. Our average ΔE_{00} color difference across the entire Macbeth chart is 3.77. Although this is above visual threshold, these differences are likely to go unnoticed in practice.

4.3.2. Qualitative Evaluation

We evaluated the robustness of the SfD camera by positioning the standard Macbeth color chart at varying distances from the calibration plane. As shown in Fig. 5a, the results indicate that the SfD camera maintains a consistent SAM level within a 30 cm range. Compared to the theoretical working distance from the calibration plane, the SfD camera demonstrates robustness even when the theoretical assumptions are mildly violated.

Fig. 5b shows that increasing the number of measurements up to 10 improves spectral reconstruction accuracy, while RGB color improvements saturate after 5 measurements. Corresponding RGB images are shown in supplement.

Fig. 6 shows several scenes assembled in the lab, illustrating spatial and spectral effects in our reconstructions. On the left we show two example measurements. From three measurements (lens positions z_2, z_3, z_5), our reconstructed RGB images show some spatial and spectral artifacts, such as the false color patterns within the black and white pinwheel target. Including additional measurements (z_7, z_8, z_9) stabilizes our inversion and removes these false color patterns, while sharpening edges and boosting saturation.

5. Conclusion

We have demonstrated Spectrum from Defocus (SfD), which reconstructs both RGB and hyperspectral images from chromatically aberrated focal stacks. Our camera, consisting of two off-the-shelf lenses and a grayscale sensor, achieves SOTA performance and fast reconstruction with an interpretable physics-based iterative algorithm.

Current limitations in this proof-of-concept prototype include its reliance on a specific PSF stack, limiting its performance to our predicted depth range and a paraxial field of view. Expanding beyond our current working volume will require a combination of both optical and algorithmic engineering, to ensure that signals of sufficient strength are available and can be recovered accurately and efficiently. Additionally, because we optimize our method for reconstruction of a high dimensional spectrum, we require > 3 measurements for RGB images. Though we ensured a fair comparison on static scenes by giving all methods the same total exposure time in simulation, an important future direction for dynamic imaging is to bring down the number of measurements needed through a combination of lower-dimensional output targets with a heavier use of training data.

References

- [1] Colorimetry part 6: Ciede2000 colour-difference formula. *International Commission on Illumination*, 2022. 7
- [2] M Kerem Aydin, Qi Guo, and Emma Alexander. Hypercolorization: propagating spatially sparse noisy spectral clues

- for reconstructing hyperspectral images. *Optics Express*, 32(7):10761–10776, 2024. 4
- [3] José M Bioucas-Dias, Antonio Plaza, Gustavo Camps-Valls, Paul Scheunders, Nasser Nasrabadi, and Jocelyn Chanussot. Hyperspectral remote sensing data analysis and future challenges. *IEEE Geoscience and remote sensing magazine*, 1(2):6–36, 2013. 1
 - [4] David Brainard. Hyperspectral image data, bear and fruit grayb, 1998. <http://color.psych.upenn.edu/hyperspectral/>. 6
 - [5] Yuanhao Cai, Jing Lin, Xiaowan Hu, Haoqian Wang, Xin Yuan, Yulun Zhang, Radu Timofte, and Luc Van Gool. Mask-guided spectral-wise transformer for efficient hyperspectral image reconstruction. In *Proceedings of the IEEE/CVF Conference on Computer Vision and Pattern Recognition*, pages 17502–17511, 2022. 2, 4
 - [6] Ayan Chakrabarti and Todd Zickler. Statistics of real-world hyperspectral images. In *CVPR 2011*, pages 193–200. IEEE, 2011. 4
 - [7] Ayan Chakrabarti and Todd Zickler. Depth and deblurring from a spectrally-varying depth-of-field. In *Computer Vision—ECCV 2012: 12th European Conference on Computer Vision, Florence, Italy, October 7–13, 2012, Proceedings, Part V 12*, pages 648–661. Springer, 2012. 3
 - [8] Stanley H Chan, Xiran Wang, and Omar A Elgendy. Plug-and-play admm for image restoration: Fixed-point convergence and applications. *IEEE Transactions on Computational Imaging*, 3(1):84–98, 2016. 4
 - [9] Inchang Choi, Daniel S Jeon, Giljoo Nam, Diego Gutierrez, and Min H Kim. High-quality hyperspectral reconstruction using a spectral prior. *ACM Transactions on Graphics*, 36(6):1–13, 2017. <https://vclab.kaist.ac.kr/siggraphasia2017p1/kaistdataset.html>. 2, 4, 5, 6
 - [10] Oliver Cossairt and Shree Nayar. Spectral focal sweep: Extended depth of field from chromatic aberrations. In *2010 IEEE International Conference on Computational Photography (ICCP)*, pages 1–8. IEEE, 2010. 3
 - [11] Yao-Ze Feng and Da-Wen Sun. Application of hyperspectral imaging in food safety inspection and control: a review. *Critical reviews in food science and nutrition*, 52(11):1039–1058, 2012. 1, 6
 - [12] Qiang Fu, Matheus Souza, Eunsue Choi, Suhyun Shin, Seung-Hwan Baek, and Wolfgang Heidrich. Limitations of data-driven spectral reconstruction—an optics-aware analysis. *CoRR*, 2024. 2, 6
 - [13] Michael E Gehm, Renu John, David J Brady, Rebecca M Willett, and Timothy J Schulz. Single-shot compressive spectral imaging with a dual-disperser architecture. *Optics express*, 15(21):14013–14027, 2007. 2
 - [14] Ralf Habel, Michael Kudenov, and Michael Wimmer. Practical spectral photography. In *Computer graphics forum*, pages 449–458. Wiley Online Library, 2012. 2
 - [15] Felix Heide, Mushfiquur Rouf, Matthias B Hullin, Bjorn Labitzke, Wolfgang Heidrich, and Andreas Kolb. High-quality computational imaging through simple lenses. *ACM Transactions on Graphics (ToG)*, 32(5):1–14, 2013. 3
 - [16] Felix Heide, Qiang Fu, Yifan Peng, and Wolfgang Heidrich. Encoded diffractive optics for full-spectrum computational imaging. *Scientific reports*, 6(1):33543, 2016. 3
 - [17] Qian Huang, Yunqian Li, Linsen Chen, Xiaoming Zhong, Jinli Suo, Zhan Ma, Tao Yue, and Xun Cao. Multispectral focal stack acquisition using a chromatic aberration enlarged camera. In *2017 IEEE International Conference on Image Processing (ICIP)*, pages 1627–1631. IEEE, 2017. 3
 - [18] Zeqiang Lai, Chenggang Yan, and Ying Fu. Hybrid spectral denoising transformer with guided attention. In *Proceedings of the IEEE/CVF International Conference on Computer Vision*, pages 13065–13075, 2023. 5
 - [19] Zhouhan Lin, Yushi Chen, Xing Zhao, and Gang Wang. Spectral-spatial classification of hyperspectral image using autoencoders. In *2013 9th international conference on information, Communications & Signal Processing*, pages 1–5. IEEE, 2013. 2
 - [20] Guolan Lu and Baowei Fei. Medical hyperspectral imaging: a review. *Journal of biomedical optics*, 19(1):010901–010901, 2014. 1
 - [21] Fulin Luo, Xi Chen, Xiuwen Gong, Weiwen Wu, and Tan Guo. Dual-window multiscale transformer for hyperspectral snapshot compressive imaging. In *Proceedings of the AAAI Conference on Artificial Intelligence*, pages 3972–3980, 2024. 2
 - [22] Jiawei Ma, Xiao-Yang Liu, Zheng Shou, and Xin Yuan. Deep tensor admm-net for snapshot compressive imaging. In *Proceedings of the IEEE/CVF International Conference on Computer Vision*, pages 10223–10232, 2019. 2
 - [23] Kristina Monakhova, Kyrollos Yanny, Neerja Aggarwal, and Laura Waller. Spectral diffusercam: lensless snapshot hyperspectral imaging with a spectral filter array. *Optica*, 7(10):1298–1307, 2020. 3, 4
 - [24] Sima Peyghambari and Yun Zhang. Hyperspectral remote sensing in lithological mapping, mineral exploration, and environmental geology: an updated review. *Journal of Applied Remote Sensing*, 15(3):031501–031501, 2021. 1
 - [25] Wallace M Porter and Harry T Enmark. A system overview of the airborne visible/infrared imaging spectrometer (aviris). In *Imaging spectroscopy II*, pages 22–31. SPIE, 1987. 2
 - [26] Vishwanath Saragadam and Aswin C Sankaranarayanan. Krism—krylov subspace-based optical computing of hyperspectral images. *ACM Transactions on Graphics (TOG)*, 38(5):1–14, 2019. 3, 4
 - [27] Robert W Slawson, Zoran Ninkov, and Elliott P Horch. Hyperspectral imaging: wide-area spectrophotometry using a liquid-crystal tunable filter. *Publications of the Astronomical Society of the Pacific*, 111(759):621, 1999. 2
 - [28] Ashwin Wagadarikar, Renu John, Rebecca Willett, and David Brady. Single disperser design for coded aperture snapshot spectral imaging. *Applied optics*, 47(10):B44–B51, 2008. 2
 - [29] Ting Xie, Licheng Liu, and Lina Zhuang. Plug-and-play priors for multi-shot compressive hyperspectral imaging. *IEEE Transactions on Image Processing*, 32:5326–5339, 2023. 2

- [30] Fumihito Yasuma, Tomoo Mitsunaga, Daisuke Iso, and Shree K Nayar. Generalized assorted pixel camera: post-capture control of resolution, dynamic range, and spectrum. *IEEE transactions on image processing*, 19(9):2241–2253, 2010. [5](#), [6](#)
- [31] Shuyue Zhan, Weiwen Zhou, Xu Ma, and Hui Huang. Hyperspectral imaging bioinspired by chromatic blur vision in color blind animals. In *Photonics*, page 91. MDPI, 2019. [2](#), [4](#), [6](#)
- [32] Yuanyuan Zhao, Xuemei Hu, Hui Guo, Zhan Ma, Tao Yue, and Xun Cao. Spectral reconstruction from dispersive blur: A novel light efficient spectral imager. In *Proceedings of the IEEE/CVF Conference on Computer Vision and Pattern Recognition*, pages 12202–12211, 2019. [2](#)